

Ab initio calculated magneto-optical Kerr effect of ferromagnetic metals: Fe and Ni

P.M. Oppeneer, T. Maurer, J. Sticht, and J. Kübler

Institut für Festkörperphysik, Technische Hochschule, D-6100 Darmstadt, Germany

(Received 25 July 1991)

We present a computational method for the *ab initio* study of magneto-optical quantities like the optical conductivity and the magneto-optical Kerr rotation based on density-functional theory. This method is tested here on the ferromagnetic metals Fe and Ni. The results for Fe agree very well with experimental data. The magneto-optical polar Kerr rotation is predicted accurately. For Ni the results are in fair agreement with experiment. In those points where deviations from experimental data are found, they can be traced back to the well-known fact that the local-density approximation is of moderate success in describing some of the Ni 3*d* bands.

I. INTRODUCTION

The magneto-optical Kerr effect (MOKE) has attracted much attention in fundamental and in applied research, because in the latter case it is technologically very promising for the realization of high density storage systems.^{1,2} Digital information, which is suitably stored in a magnetic material can be read out using MOKE. This fact has greatly stimulated the search for good magneto-optical recording materials and the magneto-optical properties of many materials were investigated. Detailed overviews were recently given by Buschow³ and by Reim and Schoenes.⁴ In spite of the intensive experimental research, the theoretical understanding of MOKE leaves a lot to be desired. For instance, the appearance of high peaks in the MOKE spectrum has been attributed to different physical origins such as interband transitions and spin-orbit coupling,^{5,6} half-metallic ferromagnetism together with spin-orbit coupling,⁷ and even to relativistic effects.⁸ A somewhat different explanation for large MOKE peaks was suggested by Feil and Haas,⁹ who argued that such peaks correspond to plasma resonance frequencies of free charge carriers.

Also, the successful description of MOKE by means of first-principles band-structure methods is as yet rather problematic. Although the absorptive parts of the optical conductivity tensor that determines the Kerr-rotation angle were calculated for elemental metals¹⁰⁻¹⁴ and some compounds,¹⁵ the polar Kerr-rotation angle itself has, to our knowledge, not yet been calculated for elemental metals, as Fe, Co, and Ni. For the case of the compound NiUSn the situation is different; here the polar Kerr rotation was computed by Daalderop *et al.*¹⁶ But these authors did not publish a test of their method on simpler systems like elemental 3*d* metals. In our opinion, these tests are essential since there are several computational difficulties inherent in MOKE calculations.

One of the main reasons for these difficulties is that for the evaluation of the Kerr rotation an accurate value of both the dispersive and absorptive part of the off-diagonal conductivity tensor needs to be known. This

quantity is difficult to calculate, as it depends crucially on small band-structure effects, like the spin-orbit coupling and exchange splitting. The absorptive part can be calculated with a standard Brillouin-zone (BZ) integration method and, in principle, the Kramers-Kronig (KK) transformation can then be used to obtain the dispersive part. However, special care is needed to achieve sufficient convergence of the KK integral. For this reason, the KK transformation is not very suitable for the *ab initio* study of MOKE.

The aim of this work is to describe an accurate, first-principles method with which detailed *ab initio* studies of MOKE can be made. The theoretical basis for our work is the density-functional theory in the local-density approximation (LDA).¹⁷ The electron bands and the electron wave function are evaluated with the augmented spherical wave (ASW) method.¹⁸ The optical conductivity tensor, which is the critical part of MOKE, is as usual calculated with the Kubo formula.¹⁹ But since it is particularly important to obtain accurate values of this quantity, we developed a special Brillouin-zone integration technique, which is better suited for the study of MOKE as the Kramers-Kronig technique. With this integration technique, lifetime effects are directly taken into account, so that an additional smoothening of results for comparison with experiment is no longer needed. Furthermore, we developed an accurate method for the computation of the optical transition matrix elements. In these points our approach differs from other computational methods and it is exactly these two points which make a detailed investigation of MOKE feasible with our method. This statement is elucidated in this paper by our results for Fe and Ni.

II. THEORY

The magneto-optical Kerr effect is found when polarized light is reflected from the surface of a magnetic material. The rotation angle of the polarization direction of

the reflected light with respect to the original polarization is the so-called Kerr angle. This angle depends in general on the relative geometry of the surface plane, the magnetization direction, and the direction of the wave vector of the incoming light. Here we shall consider only the physically interesting case, namely, the polar Kerr effect, for which both the magnetization and the incoming wave vector are perpendicular to the surface. In this case, the complex polar Kerr angle can be expressed in terms of the macroscopic conductivity tensor σ .²⁰ For cubic systems, with the z axis chosen parallel to the magnetization, the complex Kerr angle is given by⁴

$$\Phi_K \equiv \phi_K + i \epsilon_K = \frac{-\sigma_{xy}}{\sigma_{xx} \sqrt{1 + i \left(\frac{4\pi}{\omega}\right) \sigma_{xx}}} . \quad (1)$$

Here ϕ_K is the real Kerr-rotation angle, ϵ_K is the so-called Kerr ellipticity, and σ_{xx} and σ_{xy} are components of the conductivity tensor.

The macroscopic conductivity tensor in turn can be related to microscopic optical transitions with the Kubo formula.¹⁹ A clear derivation was given by Wang and Callaway,^{10,21} to whom we refer for details. The components of the interband conductivity tensor (per unit volume) can be expressed as

$$\sigma_{xy}(\omega) = \frac{i e^2}{m^2 \hbar} \sum_{\mathbf{k}} \sum_{\substack{\ell\sigma_1 \\ \text{occ}}} \sum_{\substack{n\sigma_2 \\ \text{unocc}}} \frac{1}{\omega_{n\sigma_2 \ell\sigma_1}(\mathbf{k})} \left(\frac{\Pi_{\ell\sigma_1 n\sigma_2}^x \Pi_{n\sigma_2 \ell\sigma_1}^y}{\omega - \omega_{n\sigma_2 \ell\sigma_1}(\mathbf{k}) + i\delta} + \frac{(\Pi_{\ell\sigma_1 n\sigma_2}^x \Pi_{n\sigma_2 \ell\sigma_1}^y)^*}{\omega + \omega_{n\sigma_2 \ell\sigma_1}(\mathbf{k}) + i\delta} \right), \quad (2)$$

$$\sigma_{xx}(\omega) = \frac{i e^2}{m^2 \hbar} \sum_{\mathbf{k}} \sum_{\substack{\ell\sigma_1 \\ \text{occ}}} \sum_{\substack{n\sigma_2 \\ \text{unocc}}} \frac{1}{\omega_{n\sigma_2 \ell\sigma_1}(\mathbf{k})} \left(\frac{|\Pi_{\ell\sigma_1 n\sigma_2}^x|^2}{\omega - \omega_{n\sigma_2 \ell\sigma_1}(\mathbf{k}) + i\delta} + \frac{|\Pi_{\ell\sigma_1 n\sigma_2}^x|^2}{\omega + \omega_{n\sigma_2 \ell\sigma_1}(\mathbf{k}) + i\delta} \right), \quad (3)$$

with $\delta = 1/\tau$, τ being a phenomenological relaxation time, and $\hbar\omega_{n\sigma_2 \ell\sigma_1} = E_{n\sigma_2}(\mathbf{k}) - E_{\ell\sigma_1}(\mathbf{k})$, the energy difference between an unoccupied band n with spin index σ_2 and an occupied band ℓ with spin σ_1 . The quantities $\Pi_{n\sigma_2 \ell\sigma_1}$ are matrix elements of the momentum operator

$$\begin{aligned} \Pi_{n\sigma_2 \ell\sigma_1}(\mathbf{k}) &= \int \psi_{nk\sigma_2}^*(\mathbf{r}) \left[\mathbf{p} + \left(\frac{\hbar}{4mc^2} \right) [\boldsymbol{\sigma} \times \nabla V(\mathbf{r})] \right] \\ &\quad \times \psi_{\ell k\sigma_1}(\mathbf{r}) d\mathbf{r} \end{aligned} \quad (4)$$

with $\psi_{nk\sigma_2}(\mathbf{r})$ the Bloch wave function. Apart from the interband contribution to the conductivity tensor, there is also the intraband conductivity,¹⁰ which can be described well with an empirical Drude term

$$\sigma_D(\omega) = \frac{\sigma_0}{1 - i\omega \tau_D} . \quad (5)$$

The constants σ_0 and τ_D are usually known from experiments.

So far we only summarized the standard theory for MOKE, which is used in all existing first-principles methods. It is, however, instructive to analyze first the computational difficulties that are connected with the evaluation of MOKE, so that we can elucidate why we decided to develop a computational technique. These difficulties are twofold: first there is the BZ integration needed for σ_{xx} and σ_{xy} , and second, the calculation of the matrix elements $\Pi_{n\sigma_2 \ell\sigma_1}$ need be mastered. Most of all, one would of course like to use the expressions (2) and (3) of Wang and Callaway¹⁰ directly, with the lifetime effects exactly taken into account. However, in all existing *ab initio* methods the procedure followed is different: first the limit $\delta \rightarrow 0$ is taken and then the absorptive part of

the conductivity tensor can be calculated with a standard integration routine.^{22,23} The dispersive part can then in principle be obtained by performing a KK transformation on the absorptive part, e.g.,

$$\sigma_{xy}^{(1)}(\omega) = \frac{2}{\pi} P \int_0^\infty \frac{\omega'}{\omega'^2 - \omega^2} \sigma_{xy}^{(2)}(\omega') d\omega' , \quad (6)$$

with $\sigma_{xy}^{(1)}$ and $\sigma_{xy}^{(2)}$ the real and imaginary part of σ_{xy} , respectively. At the end, the calculated spectra are smoothed again as to simulate lifetime effects and to allow for comparison with experiment. One of the problems connected with this procedure is that it is difficult to achieve convergence of the KK integral. The absorptive part of the spectrum has a very sharply peaked structure (see, for example, Fig. 1) and therefore a very dense ω mesh is needed to resolve the peaks properly. In addition to this, one has to carry the KK integration up to high frequencies, due to its slow convergence. Cutoff values of about 5 Ry are required to make the integral convergent for frequencies up to 2 Ry.¹² However, the intrinsic error in the absorptive part $\sigma_{xy}^{(2)}$ can become very large, even more than 100% for frequencies over 1 Ry. This error is caused by the second problem, the evaluation of $\Pi_{n\sigma_2 \ell\sigma_1}$. It is difficult to compute the matrix elements precisely, due to basis set incompleteness and approximations of the integrals in (4). Most first-principles methods use a set of variationally constructed, incomplete basis functions, which yield a good estimate of the band energies, but the wave functions are not as well described and this description becomes especially bad for energy bands which lie high above the Fermi energy. This leads to the fact that matrix elements belonging to such bands can easily be off by more than 100% and consequently the absorptive part of the conductivity tensor is not well

determined for high frequencies.

In order to avoid the above-mentioned problems altogether, we developed a new method to evaluate the transition matrix elements and a special BZ-integration method.^{24–26} The matrix elements are calculated as precisely as possible, although our basis set is also incomplete. Further, it is important that with our BZ-integration method, the full complex conductivity tensor is calculated directly in the form of (2) and (3), as a function of the frequency and at a fixed relaxation time. Thus, no additional smoothening of the spectra is needed. Moreover, since our spectra are smooth, we only have to perform the BZ integrals for a small number of ω points. In the following we first outline the way in which we evaluated the matrix elements and then discuss the BZ-integration method.

In the ASW method,¹⁸ as in other fast methods like the linear-muffin-tin-orbital (LMTO) method,²⁷ the unit cell is divided into an interstitial region, that nearly vanishes and where the potential is assumed to be flat, and into a collection of atomic spheres centered around the nuclei. The wave function in these two parts is written as

$$\psi_{nk\sigma}^{(\nu)}(\mathbf{r}) = \sum_{L\mu} C_{L\sigma}^{(\mu)}(n, \mathbf{k}) \left(\delta_{\nu\mu} \tilde{H}_{L\sigma}(\mathbf{r} - \boldsymbol{\tau}_\nu) + \sum_{L''} B_{L''L}(\boldsymbol{\tau}_\nu - \boldsymbol{\tau}_\mu; \mathbf{k}) \times \tilde{J}_{L''\sigma}(\mathbf{r} - \boldsymbol{\tau}_\nu) \right) \quad (7)$$

for \mathbf{r} inside the sphere centered around $\boldsymbol{\tau}_\nu$ and

$$\psi_{nk\sigma}(\mathbf{r}) = \sum_{L\mu} C_{L\sigma}^{(\mu)}(n, \mathbf{k}) \times \sum_{\mathbf{R}_j} e^{i\mathbf{k}\cdot\mathbf{R}_j} H_L(\mathbf{r} - \mathbf{R}_j - \boldsymbol{\tau}_\mu) \quad (8)$$

for \mathbf{r} in the interstitial region. Here \tilde{H} and \tilde{J} denote the augmented spherical Hankel and Bessel functions, while H denotes the unaugmented spherical Hankel functions, and σ is the spin index. B is the Korringa-Kohn-Rostoker (KKR) structure constant which is set equal to zero for $\boldsymbol{\tau}_\mu = \boldsymbol{\tau}_\nu$. Further details can be found in Ref. 18. The Schrödinger equation is solved in the scalar relativistic approximation with spin-orbit coupling included by a second variation. The spin-orbit term in $\Pi_{n\sigma_2\ell\sigma_1}$, however, is known to be much smaller than the canonical momentum operator,¹⁰ and therefore we neglect this term in (4). This means that no spin-flip transitions are taken into account, but the effect of spin-orbit coupling itself is taken into account through the band energies and the wave functions. In our approach the integral over the unit

cell (UC) naturally splits up into an integral over atomic spheres and one over the interstice. It is convenient to extend the free Hankel functions into the spheres, so that the integral can be rewritten as

$$\Pi_{n\ell\sigma}(\mathbf{k}) = -i\hbar \left(\sum_{\nu} [(\psi_{nk\sigma}^{(\nu)} | \nabla | \psi_{\ell k\sigma}^{(\nu)})_{S_\nu} - (\psi_{nk\sigma} | \nabla | \psi_{\ell k\sigma})_{S_\nu}] + (\psi_{nk\sigma} | \nabla | \psi_{\ell k\sigma})_{UC} \right), \quad (9)$$

where the parentheses stand for an integral over a sphere only. The combination of two extrapolated free Hankel functions that are both centered at $\boldsymbol{\tau}_\nu$ is to be treated differently as we will show, because such a combination would lead to divergent integrals, due to the poles of the unaugmented Hankel functions. An important consequence of rewriting the integral in this form is that the L'' sum in (7) converges much more rapidly and so an improved accuracy is gained.¹⁸ The free Hankel functions can be represented with the KKR expansion theorem¹⁸ as a sum of free Bessel functions, so that every wave function in (9) can effectively be written as a sum of a Hankel and a Bessel part. An integral in (9) thus gives four contributions, namely a Hankel-Hankel combination, a Hankel-Bessel combination, a Bessel-Hankel combination, and a Bessel-Bessel combination. Before we work out these integrals, we mention that a different derivation of the matrix elements in the ASW method was given by Rompa, Eppenga, and Schuurmans.²⁸ Their derivation leads to an expression that is more difficult to evaluate than ours; we come back to this point later.

The first term in (9) is relatively easy. The r -independent coefficients can be taken out of the integral and the integration itself can be split into a radial and an angular integration. The angular integration can be done analytically, but the radial one has to be done numerically. The second term is more complicated. The Hankel-Bessel and Bessel-Hankel combinations have poles at $r = 0$ due to singularities of the free Hankel functions. It can be shown that these poles exactly cancel and that the remaining integrals can be done analytically, using mathematical properties of Bessel and Hankel functions.²⁹ The third term can be worked out by extending the integral over the UC to an integral over \mathcal{R}^3 and then apply Green's theorem to transform the integration into an integration over infinitesimal spherical surfaces enclosing the singularities of the free Hankel functions. This procedure leads to energy derivatives of the structure constants. Our results for the matrix elements can be summarized as follows:

$$\begin{aligned} \Pi_{n\ell\sigma}(\mathbf{k}) = \hbar \sum_{\nu} \sum_{LL'} \{ & C_{L\sigma}^{(\nu)*}(\mathbf{n}\mathbf{k}) [\mathbf{M}_{LL'}^{(\nu,\sigma)}(1,1) + \mathbf{T}_{LL'}^{(\nu)}(1,1)] C_{L'\sigma}^{(\nu)}(\boldsymbol{\ell}\mathbf{k}) \\ & + C_{L\sigma}^{(\nu)*}(\mathbf{n}\mathbf{k}) [\mathbf{M}_{LL'}^{(\nu,\sigma)}(1,2) + \mathbf{T}_{LL'}^{(\nu)}(1,2) + \mathbf{P}_{LL'}(1,2)] A_{L'\sigma}^{(\nu)}(\boldsymbol{\ell}\mathbf{k}) \\ & + A_{L\sigma}^{(\nu)*}(\mathbf{n}\mathbf{k}) [\mathbf{M}_{LL'}^{(\nu,\sigma)}(2,1) + \mathbf{T}_{LL'}^{(\nu)}(2,1) + \mathbf{P}_{LL'}(2,1)] C_{L'\sigma}^{(\nu)}(\boldsymbol{\ell}\mathbf{k}) \\ & + A_{L\sigma}^{(\nu)*}(\mathbf{n}\mathbf{k}) [\mathbf{M}_{LL'}^{(\nu,\sigma)}(2,2) + \mathbf{T}_{LL'}^{(\nu)}(2,2)] A_{L'\sigma}^{(\nu)}(\boldsymbol{\ell}\mathbf{k}) \\ & + C_{L\sigma}^{(\nu)*}(\mathbf{n}\mathbf{k}) [\mathbf{Q}_{LL'}(1,2)] \dot{A}_{L'\sigma}^{(\nu)}(\boldsymbol{\ell}\mathbf{k}) \}. \end{aligned} \quad (10)$$

Here we introduced the following abbreviations:

$$A_{L\sigma}^{(\nu)}(\mathbf{n}\mathbf{k}) = \sum_{L'\mu} B_{LL'}(\tau_\nu - \tau_\mu; \mathbf{k}) C_{L'\sigma}^{(\mu)}(\mathbf{n}\mathbf{k}) \quad (11)$$

and

$$\dot{A}_{L\sigma}^{(\nu)}(\mathbf{n}\mathbf{k}) = \sum_{L'\mu} \dot{B}_{LL'}(\tau_\nu - \tau_\mu; \mathbf{k}) C_{L'\sigma}^{(\mu)}(\mathbf{n}\mathbf{k}) \quad (12)$$

with \dot{B} the energy derivative of the structure constant.¹⁸ The matrices in square brackets are numbered according to the partitioning into Hankel- and Bessel-type functions, with the convention that "1" stands for a Hankel type function and "2" for a Bessel type. The \mathbf{M} matrix is given by

$$\begin{aligned} \mathbf{M}_{LL'}^{(\nu,\sigma)}(\alpha, \beta) = & \operatorname{sgn}(\ell' - \ell) \left(\int_0^{S_\nu} dr r f_\ell^{(\alpha,\sigma)}(r) f_{\ell'}^{(\beta,\sigma)}(r) \right) \mathbf{D}_{LL'} \\ & + \operatorname{sgn}(\ell' - \ell) \left(\int_0^{S_\nu} dr r^2 f_\ell^{(\alpha,\sigma)}(r) \frac{d}{dr} f_{\ell'}^{(\beta,\sigma)}(r) \right) \mathbf{G}_{LL'} \end{aligned} \quad (13)$$

with $\alpha, \beta = 1, 2$ and $f_\ell^{(1,\sigma)}(r) = \tilde{h}_\ell^{(\sigma)}(r)$ and $f_\ell^{(2,\sigma)} = \tilde{j}_\ell^{(\sigma)}(r)$, the augmented Hankel and Bessel functions. The matrices \mathbf{G} and \mathbf{D} are defined through

$$\mathbf{G}_{LL'} = \int d\Omega Y_L(\mathbf{r}) \left(\frac{\mathbf{r}}{r} \right) Y_{L'}(\mathbf{r}), \quad (14)$$

and through

$$\mathbf{D}_{LL'} = \int d\Omega Y_L(\mathbf{r}) (r\nabla) Y_{L'}(\mathbf{r}). \quad (15)$$

We work here with real spherical harmonics and these matrices can simply be evaluated and then tabulated once and for all. The matrix \mathbf{T} is defined by

$$\begin{aligned} \mathbf{T}_{LL'}^{(\nu)}(\alpha, \beta) = & -\kappa(\kappa^{3-2\beta})^{\ell'-\ell} \\ & \times \left(\int_{\Sigma_\nu} dr r^2 f_\ell^{(\alpha)}(\kappa r) f_{\ell'}^{(\beta)}(\kappa r) \right) \mathbf{G}_{LL'} \end{aligned} \quad (16)$$

with $f_\ell^{(1)}(\kappa r) = \kappa^{\ell+1} h_\ell(\kappa r)$ and $f_\ell^{(2)}(\kappa r) = \kappa^{-\ell} j_\ell(\kappa r)$, h_ℓ and j_ℓ being the free spherical Hankel and Bessel functions, respectively, and $\kappa^2 = E$, the fixed energy parameter of the interatomic wave functions. The integration domain Σ_ν is $[0, S_\nu]$ for all Hankel-Bessel combinations, except for the Hankel-Hankel combination, for which Σ_ν is $[\infty, S_\nu]$, due to the restriction made in the derivation of (9). Analytical expressions for these integrals can be found in Ref. 29. Finally, for \mathbf{P} and \mathbf{Q} we have

$$\mathbf{P}_{LL'}(1, 2) = \mathbf{G}_{LL'} \delta_{\ell-1, \ell'}, \quad \mathbf{P}_{LL'}(2, 1) = -\mathbf{G}_{LL'} \delta_{\ell+1, \ell'}$$

whereas

$$\mathbf{Q}_{LL'} = \kappa^{\ell-\ell'+1} \mathbf{G}_{LL'} \quad (17)$$

Our expression for $\mathbf{\Pi}$ looks cumbersome, but it has several computational advantages. The matrices in square

brackets are independent of n and \mathbf{k} and therefore they have to be calculated only once. The $n\mathbf{k}$ -dependent coefficients do not require extra computer time as they are computed already in every band-structure calculation. This is an important difference with the result obtained by Rompa, Eppenga, and Schuurmans.²⁸ Their derivation leads to an expression that contains the wave-vector derivative of the structure constants, e.g., $\partial B_{LL'}/\partial \mathbf{k}$. Such a term does not appear in a standard ASW band-structure calculation and for MOKE calculations it would be necessary to compute this term additionally on many \mathbf{k} points. For this reason our expression is better suited for calculations of the conductivity tensor. Further, it is important that our matrix elements are Hermitian. This must be so on account of the general expression (4), but it is not obvious from our formula for the matrix elements (10). Nevertheless, tests showed that our matrix elements are Hermitian with an accuracy of better than 1 in 10^4 . This is an important feature of our method, because there is one approximation which is often made to evaluate $\mathbf{\Pi}_{n\ell\sigma}$, in which one neglects the integral over the interatomic region and only considers the contribution from the atomic spheres. This approximation would correspond to taking only the \mathbf{M} terms in (10) into account. We found that this approximation is generally not very good; the resulting matrix elements are not Hermitian (errors of about 20%) and the deviations from the Hermitian $\mathbf{\Pi}_{n\ell\sigma}$ are of the order of 12%. These errors partially originate from the insufficient convergence of the L sum in (11). All these problems we thus circumvent with our approach.

As mentioned before, the basis set that we use is incomplete. One way of testing the errors introduced by using an incomplete basis is to consider the diagonal matrix element, for which the following expression is valid:³⁰

$$\mathbf{\Pi}_{nn\sigma}(\mathbf{k}) = \frac{m}{\hbar} \frac{\partial E_{n\sigma}(\mathbf{k})}{\partial \mathbf{k}} \quad (18)$$

Here $E_{n\sigma}(\mathbf{k})$ are the band energies which can be deter-

mined variationally much more accurately than the wave functions. In comparing the results we obtained with (18) with those of our expression (10), we find that for energy bands below the Fermi energy the deviations are small, normally less than 7%. For energy bands above the Fermi energy, the maximal deviations increase roughly with increasing band energy, to values of about 10% for energies of 0.5 Ry above the Fermi energy. The matrix elements of bands up to 1.0 Ry above the Fermi energy deviate maximally up to 25%, while for energy bands placed 1.5 Ry above the Fermi energy the deviations can maximally be 50%. These values were obtained for monoatomic 3d metals. We note that the deviations are in general smaller for materials with several atoms in the unit cell, due to the larger basis sets that are then used. Also we remark that other methods^{31,32} do not achieve as good Π 's as ours does.

Previously, the effect of the ℓ_{\max} cutoff of the wavefunction expansion on the matrix elements was studied by Chen³¹ for the KKR method and by Uspenski *et al.*³² for the LMTO method. They both find that the matrix elements depend sensitively on the ℓ_{\max} cutoff. In going from $\ell_{\max} = 2$ to $\ell_{\max} = 4$, Chen³¹ found that the matrix elements can easily change by a factor of 2 or 3. Uspenski *et al.*³² found that for $\ell_{\max} = 2$ the calculated intraband matrix elements can be 2 or 3 times smaller than those obtained from the band energies with (18), even for energy bands below the Fermi energy. For $\ell_{\max} = 3$ they find that this deviation is already much smaller, less than 10% for energy bands below the Fermi energy. In our case, the deviations of the diagonal elements obtained by (10) and by (18) are nearly the same for $\ell_{\max} = 2$ and $\ell_{\max} = 3$, and thus our matrix elements are converged already for a cutoff of $\ell_{\max} = 2$. This is due to the special treatment of the free Hankel and Bessel functions in (9), and it implies that we have achieved convergence with respect to the ℓ summations in our expression (10) for Π .

Since the BZ-integration technique is an important element of our method, we briefly outline this technique now. It is originally due to Coleridge, Molenaar, and Lodder,²⁴ while modifications and extensions were made by Oppeneer and Lodder.²⁵ It is an analytical tetrahedron method, in which an integrand of the form $F(\mathbf{k})/G(\mathbf{k})$ is approximated within one tetrahedron by the quotient of two linear functions, the linear approximations to F and G , respectively. This approach is well suited for the evaluation of integrands with poles, as is the case of the conductivity tensor. Furthermore, as the integration is good for complex functions, we can evaluate σ_{xx} and σ_{xy} [Eqs. (2) and (3)] with a lifetime parameter explicitly included. At a given frequency, this method yields therefore directly the real and imaginary part and thus the absorptive and dispersive part of the conductivity tensor without KK transformation. An important feature is, furthermore, that in the limit of $\delta \rightarrow 0$ the method gives the correct answer, which is nontrivial, as effectively a pole in the complex plane is approached.²⁶ This feature allows us to check our results for $\delta \rightarrow 0$ against those that were computed previously with standard integration methods. The accuracy of an integra-

tion depends of course on the number of mesh points, but normally for 512 tetrahedra in the irreducible wedge of the BZ, this technique achieves accuracies better than 2%. This was established by tests against the simple cubic Green function for which analytic results are known.³³ In the neighborhood of a van Hove singularity the accuracy is less good, with deviations of about 4%. Since we normally work with finite lifetimes, these van Hove singularities do not affect our accuracy. The only disadvantage of this integration method is that it requires more computer time per integration than other tetrahedron methods,^{22,23} due to the more complicated nature of the formulas.²⁵ This, however, bears no weight against the many more BZ integrals that are needed for the dense ω mesh of the KK integrals. In concluding, we feel that this integration technique has precisely those features which are desirable for the study of MOKE.

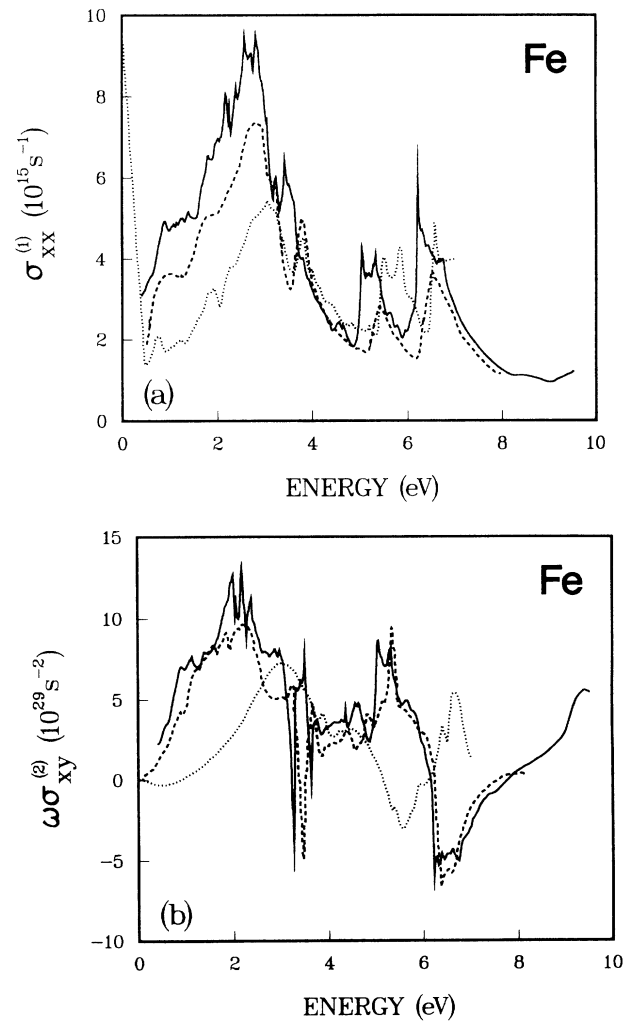


FIG. 1. The absorptive parts of the conductivity tensor of Fe, with (a) $\sigma_{xx}^{(1)}$ and (b) $\omega\sigma_{xy}^{(2)}$, as calculated by several authors. Results shown are as follows: solid curve, this work; dashed curve, Uspenski and Khalilov (Ref. 36); dotted curve, Ebert, Strange, and Gyorffy (Ref. 13) for $\sigma_{xx}^{(1)}$ and Ebert (Ref. 34) for $\omega\sigma_{xy}^{(2)}$.

III. RESULTS

With the method outlined in the previous section, we computed the conductivity tensors of Fe and Ni in the limit of infinite relaxation times, i.e., $\delta \rightarrow 0$. Previously, the absorptive parts of σ_{xx} and σ_{xy} were calculated by several authors, so that we can compare our results. For Fe, the real part of σ_{xx} ($\sigma_{xx}^{(1)}$) and the imaginary part of σ_{xy} ($\sigma_{xy}^{(2)}$) were calculated by Ebert and co-workers^{13,34} with the spin-polarized relativistic LMTO method³⁵ and by Uspenski and Khalilov³⁶ with a scalar-relativistic version of the LMTO method.²⁷ Results of the different computations are shown in Figs. 1(a) and 1(b). For $\sigma_{xx}^{(1)}$, the features of the spectra are clearly similar in all three calculations. Our results and that of Ebert, Strange, and Gyorffy¹³ appear to be shifted with respect to each other, which might be due to different lattice constants. We used here the experimental value of $a = 5.4163a_0$. For

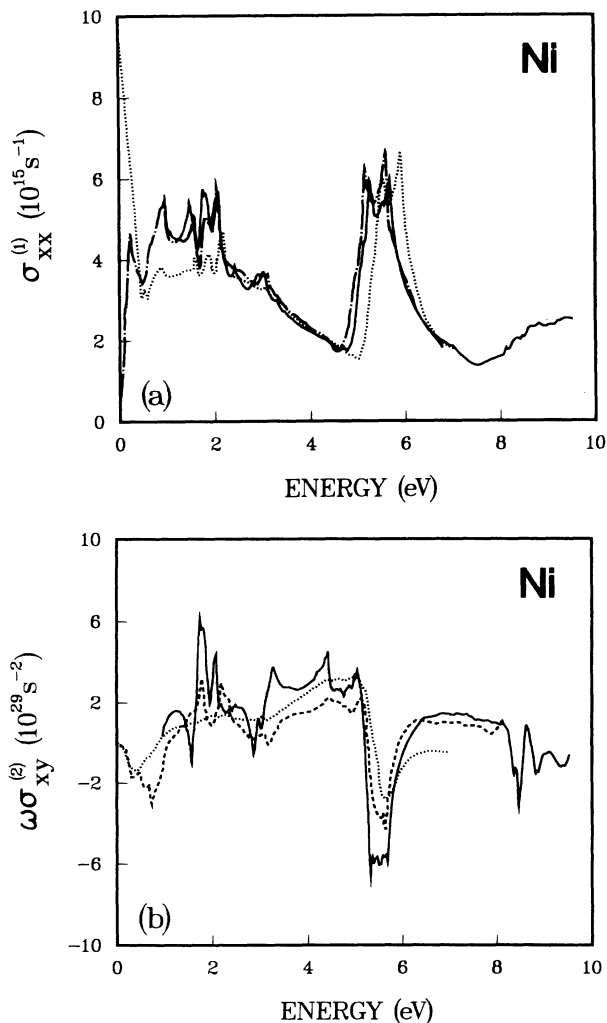


FIG. 2. As in Fig. 1, but for Ni. Results shown are as follows: solid curve, this work; dashed-dotted curve, Wang and Callaway (Ref. 10) for $\sigma_{xx}^{(1)}$; dashed curve, Uspenski and Khalilov (Ref. 36) for $\omega\sigma_{xy}^{(2)}$; dotted curve, Ebert, Strange, and Gyorffy (Ref. 13) for $\sigma_{xx}^{(1)}$ and Ebert (Ref. 34) for $\omega\sigma_{xy}^{(2)}$.

$\omega\sigma_{xy}^{(2)}$, the result of Uspenski and Khalilov³⁶ and ours compare very well, but the result of Ebert³⁴ has a different structure. He smoothed his curve, so that the sharp peaks disappeared, but apparently the hump at 2 eV is shifted to 3 eV, while the peak at 5 eV is missing in his result.

The results for Ni are shown in Figs. 2(a) and 2(b). In this case we can compare with results obtained by Wang and Callaway¹⁰ and again with those of Ebert and co-workers^{13,34} and of Uspenski and Khalilov.³⁶ Our results for $\sigma_{xx}^{(1)}$ and that of Wang and Callaway¹⁰ are nearly identical, while there is also a close resemblance with Ebert, Strange, and Gyorffy.¹³ Also for the off-diagonal conductivity $\omega\sigma_{xy}^{(2)}$, there appears to be a very good agree-

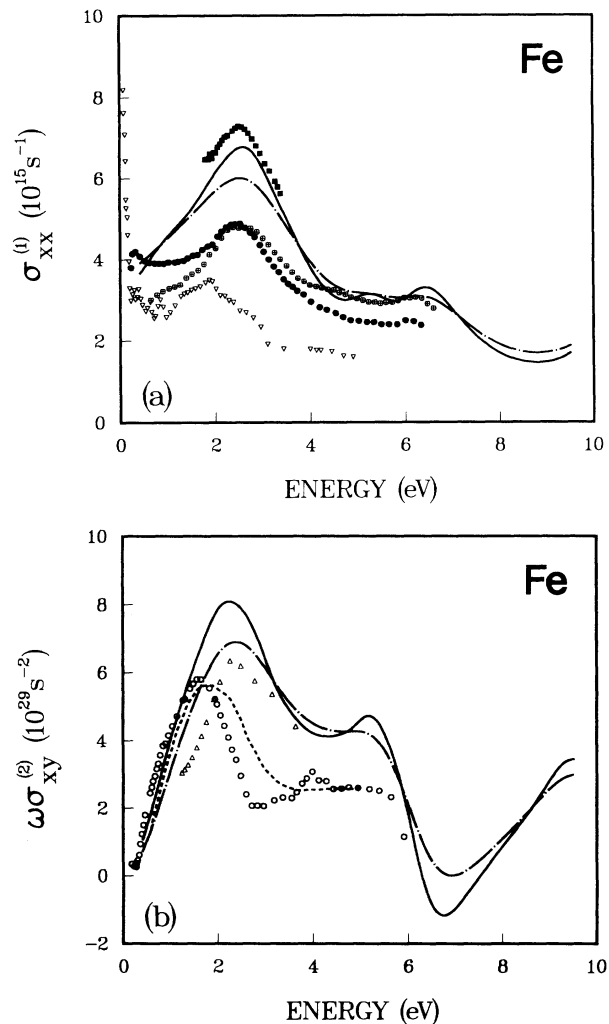


FIG. 3. Experimental and calculated results for (a) $\sigma_{xx}^{(1)}$ and (b) $\omega\sigma_{xy}^{(2)}$ of Fe. Experimental data shown for $\sigma_{xx}^{(1)}$ (a) are as follows: (■) Yolken and Kruger (Ref. 39), (∇) Bolotin, Kirillova, and Mayevskiy (Ref. 40), (⊕) Johnson and Christy (Ref. 41), and (●) Weaver *et al.* (Ref. 42). For $\omega\sigma_{xy}^{(2)}$ (b) the experimental data shown are as follows: dashed line, van Engen (Ref. 43); (o) Krinchik and Artem'ev (Ref. 44); and (Δ) Ferguson and Romagnoli (Ref. 45). Calculated results are given for two inverse lifetimes, $\delta = 0.03$ Ry for the full curve and $\delta = 0.05$ Ry for the dashed-dotted curve.

ment between the three calculations. As a first result, we conclude that our technique yields conductivity tensors which are trustworthy as far as the evaluation within energy band theory is concerned.

In order to use our method for *ab initio* predictions of MOKE, it is important that the calculations are also capable of giving a good description of experimental optical conductivities. It is found experimentally that lifetime effects play a considerable role in optical transitions. Excited states do not have an infinite lifetime, but due to many-body effects they decay after a certain time. The lifetimes are state dependent, since high-lying energy states are found to be more unstable and to have shorter lifetimes.³⁷ In principle it is even possible for us to use state-dependent lifetimes. But the difficulty is that as yet not much is known about such relaxation times. Therefore we use here one fixed relaxation time for all en-

ergy bands. These fixed relaxation times were estimated from the intraband relaxation times τ_D [see Eq. (5)] for which experimental values exist.³⁸ We assumed that the interband lifetimes are equal to or slightly smaller than the intraband lifetimes. Our results for Fe are compared in Figs. 3(a) and 3(b) with the experimental data of several authors.^{39–42} The inverse relaxation times used were $\delta = 0.03$ Ry and $\delta = 0.05$ Ry. The inclusion of lifetime effects clearly broadens and smoothens the sharp peaks in the spectra of Fig. 1. Although the exact height of the peak at 2.5 eV in $\sigma_{xx}^{(1)}$ is experimentally uncertain, we can nevertheless conclude that our curves represent the shape of the experimental data quite well. The steep increase in the experimental $\sigma_{xx}^{(1)}$ (Ref. 40) below 0.5 eV is caused by the intraband Drude behavior. A Drude term was not added in our calculation of $\sigma_{xx}^{(1)}$, but we

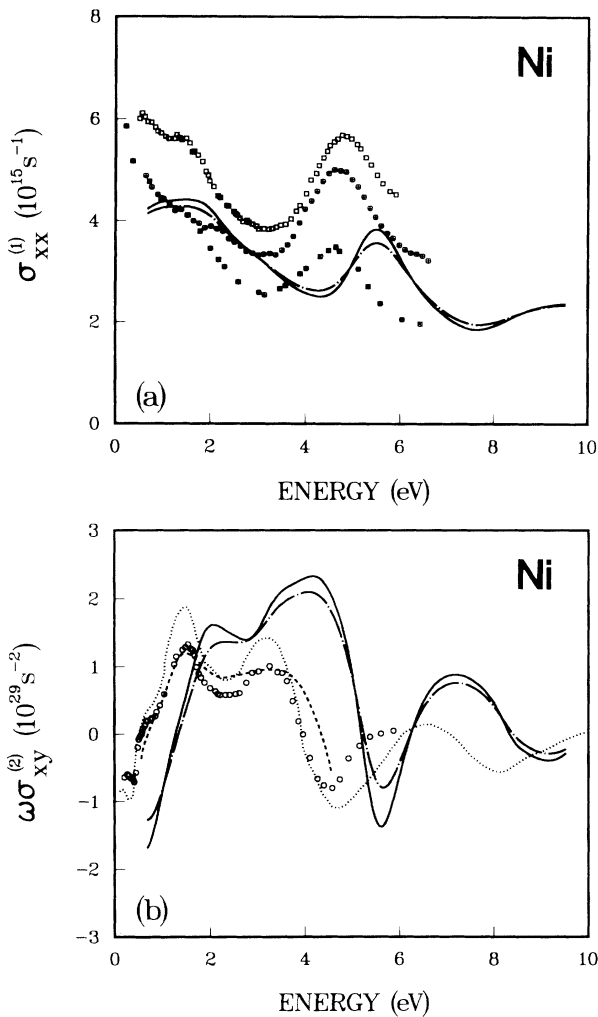


FIG. 4. As Fig. 3, but for Ni. Experiments shown for $\sigma_{xx}^{(1)}$ (a) are (\oplus) Johnson and Christy (Ref. 41), (\otimes) Ehrenreich, Phillip, and Olechna (Ref. 46), and (\square) Shiga and Pells (Ref. 47). For $\omega\sigma_{xy}^{(2)}$ (b) the experimental data are as follows: dashed line, van Engen (Ref. 43); (\circ) Krinchik and Artem'ev (Ref. 44), and dotted line, Erskine (Ref. 48). The inverse lifetimes used for the calculated results were $\delta = 0.03$ Ry for the full curve and $\delta = 0.04$ Ry for the dashed-dotted curve.

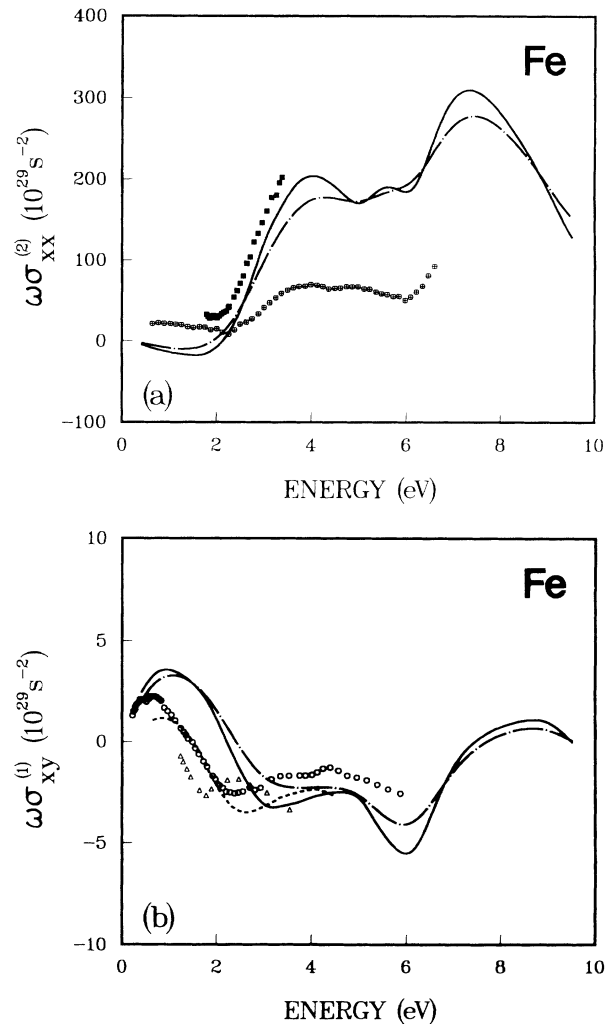


FIG. 5. Results for the dispersive parts of the conductivity tensor of Fe, with (a) $\omega\sigma_{xx}^{(2)}$ and (b) $\omega\sigma_{xy}^{(1)}$, respectively. Experimental data shown are those of (\blacksquare) Yolken and Kruger (Ref. 39) and (\oplus) Johnson and Christy (Ref. 41) for $\omega\sigma_{xx}^{(2)}$ (a), and for $\omega\sigma_{xy}^{(1)}$ (b) those of (\triangle) Ferguson and Romagnoli (Ref. 45); dashed line, van Engen (Ref. 43); and (\circ) Krinchik and Artem'ev (Ref. 44). The calculated results are as given in Fig. 3.

shall take it into account for MOKE later. For $\omega\sigma_{xy}^{(2)}$ our curves resemble the experimental data, but they predict higher values than the measurements.

Results for Ni are shown in Figs. 4(a) and 4(b). The relaxation times used were $\delta = 0.03$ Ry and $\delta = 0.04$ Ry. Again the experimental features can be recognized in the calculated spectra, but the position of the calculated peak in $\sigma_{xx}^{(1)}$ at 5.5 eV is off by about 1 eV. The dip in $\omega\sigma_{xy}^{(2)}$ is similarly displaced by 1 eV, while also the structure at 1–2 eV appears to be slightly shifted. We could trace the origin of this discrepancy by plotting $\sigma_{xx}^{(1)}$ band by band. The $X_{1\downarrow}, X_{1\uparrow}$ bands are responsible for the calculated peak at 5.5 eV. The position of these bands as calculated within the local-density approximation is not in accordance with the findings of angle-resolved photoemission measurements.^{49,50} Photoemission measurements place these bands about 1 eV higher than LDA

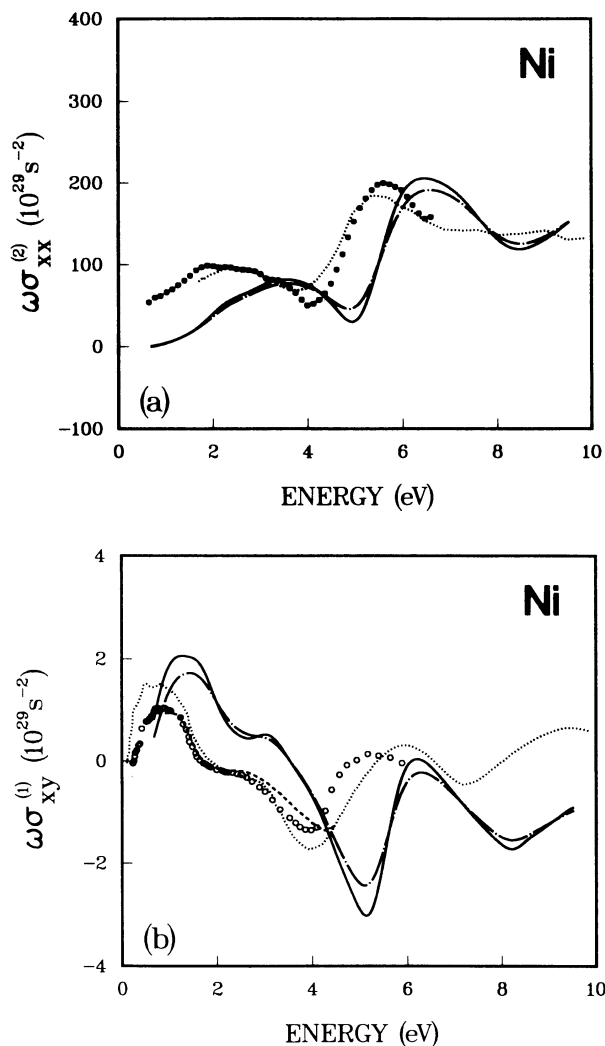


FIG. 6. As Fig. 5, but for Ni. The experimental data shown for $\omega\sigma_{xx}^{(2)}$ are as follows: dotted line, Ehrenreich, Phillip, and Olechna (Ref. 46); \oplus Johnson and Christy (Ref. 41); and for $\omega\sigma_{xy}^{(1)}$ are as follows: dashed line, van Engen (Ref. 43); \circ Krinchik and Artem'ev (Ref. 44); and dotted line, Erskine (Ref. 48). Calculated results are as given in Fig. 4.

band-structure calculations do.^{50,51} This failure of LDA for the description of these correlated Ni bands was intensively studied and its physical origin is understood.⁵² This implies that the differences between experimental results and the calculated curves in Fig. 4 are not due to our computational method, but are caused by the LDA.

In Fig. 5 we present *ab initio* calculations of $\omega\sigma_{xx}^{(2)}$ (a) and $\omega\sigma_{xy}^{(1)}$ (b) of Fe. The relaxation times were the same as used for the absorptive parts and no empirical intra-band conductivities were added. Just like $\sigma_{xx}^{(1)}$, the experimental values of $\omega\sigma_{xx}^{(2)}$ (a) spread widely. This could be caused by different surface preparation techniques, since the surface of Fe is sensitive to oxidation. For $\omega\sigma_{xy}^{(1)}$ of Fe [Fig. 5(b)] the agreement with experiment is quite satisfactory. The results for $\omega\sigma_{xx}^{(2)}$ and $\omega\sigma_{xy}^{(1)}$ of Ni are shown in Figs. 6(a) and 6(b), respectively. The overall trend seen in Fig. 6 is analogous to what was found for the absorptive parts (Fig. 4): the calculated conductivities resemble the experimental data quite well, but the structure around 5 eV appears to be displaced by about 1 eV.

Finally, the polar Kerr rotation was calculated from σ_{xx} and σ_{xy} with Eq. (1). The results for Fe are shown in Fig. 7 and those for Ni in Fig. 8. We note that in both cases the experimental data^{43,53,54} are in close agreement with each other. This indicates that these data are reproducible and reliable, which is not always obvious, since magneto-optical measurements tend to depend strongly on the surface preparation of the sample (see, e.g., Ref. 43). For Fe, our results agree very well with experiments, both for the used inverse relaxation time of $\delta = 0.03$ Ry and for $\delta = 0.05$ Ry. Apparently the precise value of δ is not so critical for the calculated Kerr rotation of

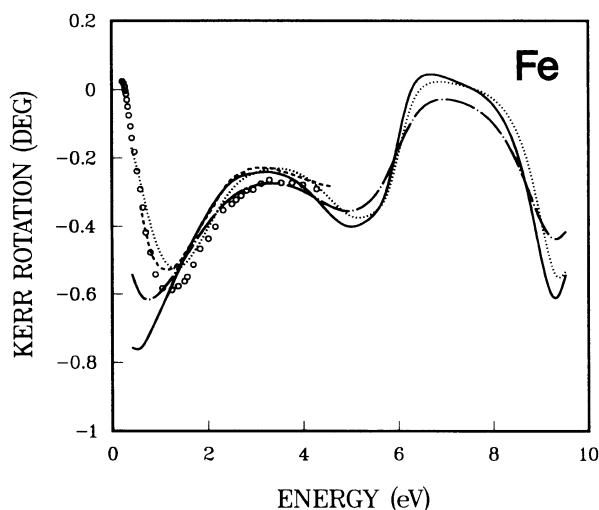


FIG. 7. Experimental and calculated results for the Kerr rotation of Fe. Experiments shown are those of \circ Krinchik and Artem'ev (Ref. 54) and dashed line, van Engen (Ref. 43). Calculated results are given for two inverse lifetimes, $\delta = 0.03$ Ry for the full curve and $\delta = 0.05$ Ry for the dashed-dotted curve. The effect of an empirical Drude conductivity on the calculated Kerr rotation is illustrated by the dotted curve, which is the result (for $\delta = 0.03$ Ry) with Drude term (Ref. 38).

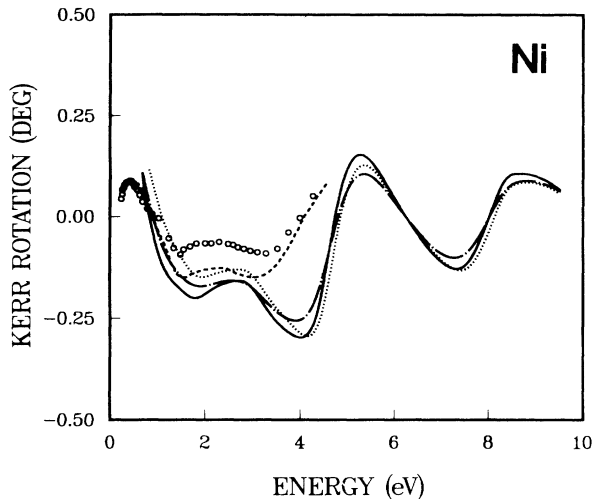


FIG. 8. Experimental and calculated results for the Kerr rotation of Ni. Experimental data shown are as follows: (o) Krinchik and Artem'ev (Ref. 54) and dashed line, van Engen, Buschow, and Erman (Ref. 53). The full curve is the calculated result with lifetime parameter $\delta = 0.03$ Ry, while the dashed-dotted curve is the result for $\delta = 0.04$ Ry. The influence of an empirical Drude conductivity (Ref. 38) on the calculated Kerr rotation of $\delta = 0.03$ Ry is illustrated by the dotted curve.

Fe. We also added an empirical intraband Drude conductivity to the calculated interband conductivity with the optical constants σ_0 and τ_D [see Eq. (5)] taken from experiment.³⁸ The effect of the intraband Drude conductivity is illustrated by the dotted curve in Fig. 7. This curve shows the calculated Kerr rotation for $\delta = 0.03$ Ry with the Drude term. The results for Ni (Fig. 8) are more difficult to interpret than those of Fe. Below 3.5 eV the calculated Kerr rotations have the same structure as the measured ones, but for higher energies there is hardly any correspondence. The difference seen around 4.5 eV beautifully illustrates the effect of the shifted peaks in σ_{xx} and σ_{xy} on the Kerr angle. The calculated $\omega\sigma_{xy}$ has no dip at 4.5 eV [Fig. 4(b)], but rather a maximum, while σ_{xx} has no peak at 4.5 eV, but more a local minimum. This changes the Kerr rotation at 4–5 eV completely and instead of a decreasing Kerr angle we obtain the opposite behavior.

IV. DISCUSSION

From Fig. 7 we conclude that the *ab initio* calculated Kerr rotation of Fe is in excellent agreement with experimental data. The calculated Kerr angles of Ni are in good agreement with experiments for energies below 3.5 eV, but for higher energies they deviate markedly from experiments. This deviation could be attributed to the fact that the LDA is only of moderate success in describing some Ni 3d bands. In conclusion, these results illustrate that our method is capable of giving *ab initio* predictions of MOKE.

In the following we wish to discuss the limitations of our approach. As we mentioned before, the accuracy of the method is satisfactorily good for energies below 0.5

Ry. Above 0.5 Ry the transition matrix elements are less accurate, due to basis set incompleteness. Likewise, the accuracy of the Kerr rotation is only reasonable for higher energies. Another point one has to be aware of is the dependence of the conductivity tensors on lattice constants. Changing the lattice constant changes the positions of the peaks in the conductivity spectra, and consequently, the position of peaks in MOKE are shifted. The size of this effect was investigated experimentally for Ni, where shifts of 0.5 eV were found.⁴⁷ By doing calculations for different lattice constants, we examined this effect theoretically and found exactly the same behavior. Therefore, for detailed predictions or for comparison with experiments, a precise knowledge of the lattice constant or the temperature is required. In addition to this, we wish to stress that we are essentially calculating bulk quantities. Many MOKE measurements are made on thin films, for which our technique can at best give an estimate only. As we noted before, a further restriction is posed by strong electron correlations. The LDA description of correlated electron bands is only modestly good and therefore one cannot expect that the calculated Kerr rotations of correlated materials are very accurate. Difficulties with strong electron correlations can, however, be recognized before hand, since one usually knows in which materials strong correlations can be anticipated.

Previously, a number of explanations of MOKE were discussed in the literature.^{3–9,16,43} From the outcome of the calculations we can contribute to these viewpoints. In the first place, our results confirm that MOKE depends primarily on spin-orbit interaction. In test calculations without spin-orbit coupling we obtained $\sigma_{xy}(\omega) = 0.0$ for the interband part, a result which was also expected on theoretical grounds.⁵ Also, we find that the magnitude of the Kerr rotation scales in proportion to the spin-orbit coupling strength. Nonetheless, spin-orbit interaction in itself is not sufficient for large MOKE peaks. The strength of the spin-orbit coupling in Fe and Ni is actually of similar size,⁵⁵ but the Kerr rotation of Fe is about 3–6 times larger than of Ni. As a second result, our calculations show that this difference is due to the positions of occupied and unoccupied bands in the BZ and the detailed exchange splitting. Thus, the basic origin of MOKE appears to be interband transitions in combination with spin-orbit coupling and exchange splitting, as proposed by several authors.^{5,6,20} The validity of the interband picture for these metals was previously unclear, mainly because other calculations that used electron bands which were fitted to photoemission data, gave results for σ_{xy} of Ni which were in complete disagreement with experiment.⁵¹ Contrary to these findings, however, our calculations show that the interband model can indeed give a reliable description of MOKE. We further found that intraband effects are not unimportant, but their influence on the MOKE spectrum is restricted to energies smaller than 1–2 eV (see Fig. 7). Other mechanisms, like the plasma-resonance model of Feil and Haas⁹ could not be confirmed in the present study, but neither can they be completely excluded. Similarly, the explanations for the occurrence of large Kerr rotations in Heusler alloys as given by de Groot *et al.*⁷ and Wijngaard, Haas,

and de Groot⁸ can be verified only by calculations for these alloys, which we intend to carry out in the future.

ACKNOWLEDGMENTS

One of the authors (J.K.) is grateful for the hospitality and support provided by IBM–Yorktown Heights, where

this work was initiated. He is indebted to A.R. Williams and R.J. Gambino for numerous interesting discussions. J.S. thanks the IBM–Almaden Research Center for offering him the opportunity to perform further research in this field. This work was partially supported by the Sonderforschungsbereich 252 Darmstadt/Frankfurt/Mainz.

- ¹M.H. Kryder, *J. Appl. Phys.* **57**, 3913 (1985).
²W.H. Meiklejohn, *Proc. IEEE* **74**, 1570 (1986).
³K.H.J. Buschow, in *Ferromagnetic Materials*, edited by E.P. Wohlfahrt and K.H.J. Buschow (North-Holland, Amsterdam, 1988), Vol. 4, pp. 493–595.
⁴W. Reim, *J. Magn. Magn. Mater.* **58**, 1 (1986); W. Reim and J. Schoenes, in *Ferromagnetic Materials*, edited by E.P. Wohlfahrt and K.H.J. Buschow (North-Holland, Amsterdam, 1990), Vol. 5, pp. 133–236.
⁵H.S. Bennett and E.A. Stern, *Phys. Rev.* **137**, A448 (1965).
⁶B.R. Cooper, *Phys. Rev.* **139**, A1504 (1965); J.L. Erskine and E.A. Stern, *Phys. Rev. B* **8**, 1239 (1973).
⁷R.A. de Groot, F.M. Mueller, P.G. van Engen, and K.H.J. Buschow, *Phys. Rev. Lett.* **50**, 2024 (1983); *J. Appl. Phys.* **55**, 2151 (1984).
⁸J.H. Wijngaard, C. Haas, and R.A. de Groot, *Phys. Rev. B* **40**, 9318 (1989).
⁹H. Feil and C. Haas, *Phys. Rev. Lett.* **58**, 65 (1987).
¹⁰C.S. Wang and J. Callaway, *Phys. Rev. B* **9**, 4897 (1974).
¹¹M. Singh, C.S. Wang, and J. Callaway, *Phys. Rev. B* **11**, 287 (1975); A.R. Jani, N.E. Brener, and J. Callaway, *ibid.* **38**, 9425 (1988).
¹²E.G. Maksimov, I.I. Mazin, S.N. Rashkeev, and Y.A. Uspenski, *J. Phys. F* **18**, 833 (1988).
¹³H. Ebert, P. Strange, and B.L. Gyorffy, *J. Phys. (Paris) Colloq.* **49**, 31 (1988).
¹⁴Bong-Soo Kim, B.N. Harmon, and D.W. Lynch, *Phys. Rev. B* **39**, 5754 (1989).
¹⁵Kwang Joo Kim, B.N. Harmon, Liang-Yao Chen, and D.W. Lynch, *Phys. Rev. B* **42**, 8813 (1990); C. Koenig and D. Knab, *Solid State Commun.* **74**, 11 (1990).
¹⁶G.H.O. Daalderop, F.M. Mueller, R.C. Albers, and A.M. Boring, *J. Magn. Magn. Mater.* **74**, 211 (1988).
¹⁷A.R. Williams and U. von Barth, in *Theory of the Inhomogeneous Electron Gas*, edited by S. Lundqvist and N.H. March (Plenum, New York, 1983), p. 189.
¹⁸A.R. Williams, J. Kübler, and C.D. Gelatt, *Phys. Rev. B* **19**, 6094 (1979).
¹⁹R. Kubo, *J. Phys. Soc. Jpn.* **12**, 570 (1957).
²⁰J.L. Erskine and E.A. Stern, *Phys. Rev. B* **12**, 5016 (1975).
²¹J. Callaway *Quantum Theory of the Solid State, Part B* (Academic, New York, 1974), p. 528.
²²O. Jepsen and O.K. Andersen, *Solid. State Commun.* **9**, 1763 (1971).
²³G. Lehmann and M. Taut, *Phys. Status Solidi B* **54**, 469 (1972).
²⁴P.T. Coleridge, J. Molenaar, and A. Lodder, *J. Phys. C* **15**, 6943 (1982).
²⁵P.M. Oppeneer and A. Lodder, *J. Phys. F* **17**, 1885 (1987).
²⁶S. Kaprzyk and P.E. Mijnarends, *J. Phys. C* **19**, 1283 (1986).
²⁷O.K. Andersen, *Phys. Rev. B* **12**, 3060 (1975).
²⁸H.W.A.M. Rompa, R. Eppenga, and M.F.H. Schuurmans, *Physica* **145B**, 5 (1987).
²⁹P.M. Morse and H. Feshbach, *Methods of Theoretical Physics* (McGraw-Hill, New York, 1953), Vol. II, p. 1573.
³⁰E.I. Blount, in *Solid State Physics*, edited by F. Seitz and D. Turnbull (Academic, New York, 1962), Vol. 13, p. 305.
³¹A.B. Chen, *Phys. Rev. B* **14**, 2384 (1976).
³²Y.A. Uspenski, E.G. Maksimov, S.N. Rashkeev, and I.I. Mazin, *Z. Phys. B* **53**, 263 (1983).
³³T. Morita and T. Horiguchi, *J. Math. Phys.* **12**, 981 (1971).
³⁴H. Ebert, Habilitation thesis, University of Munich, 1990.
³⁵H. Ebert, *Phys. Rev. B* **38**, 9390 (1988).
³⁶Y.A. Uspenski and S.V. Khalilov, *Zh. Eksp. Teor. Fiz.* **95**, 1022 (1989) [*Sov. Phys. JETP* **68**, 588 (1989)].
³⁷A. Santoni and F.J. Himpsel, *Phys. Rev. B* **43**, 1305 (1991).
³⁸A.P. Lenham and D.M. Treherne, in *Optical Properties and Electronic Structure of Metals and Alloys*, edited by F. Abelès (North-Holland, Amsterdam, 1966), p. 196. Later these authors published corrected optical data [*J. Opt. Soc. Am.* **56**, 1137 (1966)], but they did not publish adjusted Drude constants. For Fe we used their Drude constants, but for Ni we used $\sigma_0 = 5 \times 10^{15} \text{ s}^{-1}$ and $\delta_D = 0.027 \text{ Ry}$, since the published σ_0 appears to be too large.
³⁹H.T. Yolken and J. Kruger, *J. Opt. Soc. Am.* **55**, 892 (1965).
⁴⁰G.A. Bolotin, M.M. Kirillova, and V.M. Mayevskiy, *Fiz. Met. Metalloved.* **27**, 224 (1969).
⁴¹P.B. Johnson and R.W. Christy, *Phys. Rev. B* **9**, 5056 (1974).
⁴²J.H. Weaver, E. Colavita, D.W. Lynch, and R. Rosei (unpublished).
⁴³P.G. van Engen, Ph.D. thesis, Technical University Delft, 1983. The results of this work can also be found in Ref. 3.
⁴⁴G.S. Krinchik and V.A. Artem'ev, *J. Appl. Phys.* **39**, 1276 (1968).
⁴⁵P.E. Ferguson and R.J. Romagnoli, *J. Appl. Phys.* **40**, 1236 (1969).
⁴⁶H. Ehrenreich, H.R. Philipp, and D.J. Olechna, *Phys. Rev.* **131**, 2469 (1963).
⁴⁷M. Shiga and G.P. Pells, *J. Phys. C* **2**, 1847 (1969).
⁴⁸J.L. Erskine, *Physica* **89B**, 83 (1977).
⁴⁹E. Dietz, U. Gerhardt, and C.J. Maetz, *Phys. Rev. Lett.* **40**, 892 (1978).
⁵⁰F.J. Himpsel, J.A. Knapp, and D.E. Eastman, *Phys. Rev. B* **19**, 2919 (1979).
⁵¹N.V. Smith, R. Lässer, and S. Chiang, *Phys. Rev. B* **25**, 793 (1982).
⁵²A. Liebsch, *Phys. Rev. Lett.* **43**, 1431 (1979).
⁵³P.G. van Engen, K.H.J. Buschow, and M. Erman, *J. Magn. Magn. Mater.* **30**, 374 (1983).
⁵⁴G.S. Krinchik and V.A. Artem'ev, *Zh. Eksp. Teor. Fiz.* **53**, 1901 (1967) [*Sov. Phys. JETP* **26**, 1080 (1968)].
⁵⁵F. Herman and S. Skillman, *Atomic Structure Calculations* (Prentice-Hall, Englewood Cliffs, NJ, 1963).